Polymerization force-regulated actin filament-Arp2/3 complex interaction dominates self-adaptive cell migrations

Xindong Chen [1,2 *], Yuhui Li [3], Ming Guo [4], Bowen Xu [1], Yanhui Ma [2], Hanxing Zhu [2 *], Xi-Qiao Feng[1*]

[1] Institute of Biomechanics and Medical Engineering, AML, Department of Engineering Mechanics, Tsinghua University, Beijing 100084, China

[2] School of Engineering, Cardiff University, Cardiff CF24 3AA, UK

[3] Univ. Grenoble-Alpes, CEA, CNRS, INRA, Interdisciplinary Research Institute of Grenoble, Laboratoire de Phyiologie Cellulaire & Végétale, CytoMorpho Lab, 38054 Grenoble, France.

[4] Department of Mechanical Engineering, Massachusetts Institute of Technology, Cambridge, MA 02139, USA

[*] Corresponding authors: chenxin7@tsinghua.edu.cn; zhuh3@cardiff.ac.uk; fengxq@tsinghua.edu.cn;

Classification: cell mechanics, biophysics and cell migration.

Keywords: propulsive force, Arp2/3 complex, branched actin filaments, self-adaptive cell migrations, extracellular microenvironments.

Abstract

Cells migrate by adapting their leading-edge behaviours to heterogeneous extracellular microenvironments (ECMs) during cancer invasions and immune responses. Yet it remains poorly understood how such complicated dynamic behaviours emerge from millisecond-scale assembling activities of protein molecules, which are hard to probe experimentally. To address this gap, we establish a spatiotemporal "resistance-adaptive propulsion" theory based on the protein interactions between Arp2/3 complexes and polymerizing actin filaments, and a multiscale dynamic modelling system spanning from molecular proteins to the cell. Combining spatiotemporal simulations with experiments, we quantitatively find that cells can accurately self-adapt propulsive forces to overcome heterogeneous ECMs via a resistance-triggered positive feedback mechanism, dominated by polymerization-induced actin filament bending and the bending-regulated actin-Arp2/3 binding. However, for high resistance regions, resistance triggered a negative feedback, hindering branched filament assembly, which adapts cellular morphologies to circumnavigate the obstacles. Strikingly, the synergy of the two opposite feedbacks not only empowers the cell with both powerful and flexible migratory capabilities to deal with complex ECMs but also enables efficient utilization of intracellular proteins by the cell. In addition, we identify that the nature of cell migration velocity depending on ECM history stems from the inherent temporal hysteresis of cytoskeleton remodeling. We also show that directional cell migration is dictated by the competition between the local stiffness of ECMs and the local polymerizing rate of actin network caused by chemotactic cues. Our results reveal that it is the polymerization force-regulated actin filament-Arp2/3 complex binding interaction that dominates self-adaptive cell migrations in complex ECMs, and we provide a predictive theory and a spatiotemporal multiscale modeling system at the protein level.

Significance

Understanding how migrating cells mechano-sense complex extracellular microenvironment (ECM) and make adaptive responses based on protein behaviors is an important yet challenging issue. By combining spatiotemporal biophysical theory derivation, protein-protein interaction analysis and dynamic multiscale modelling with experimental living imaging, we find, for the first time, that actin filament polymerization force regulates the binding affinity of Arp2/3 complex and thereby dominates self-adaptive cell migrations in ECMs via positive and negative feedbacks. Cells can sense the intensities of ECM resistances through the polymerization-induced bending states of actin filaments, and accurately determine appropriate force generations and migratory responses through the bending-regulated binding interactions of Arp2/3 complex. We demonstrate that branched actin filaments can adaptively generate propulsive force, and reveal its underlying mechanism.

Introduction

Cells migrate through coupling their propulsive forces generated by assembling cytoskeletons to extracellular microenvironments (ECMs) (1-4). Actin-based lamellipodia protrusion is a powerful force-generating system that drives cell migrations during cancer invasion, immune surveillance, and embryonic development (1, 5-9). Arp2/3 complex binds on an existing actin filament and then nucleates a daughter filament, assembling into branched actin networks in lamellipodia and invadopodia (10, 11). The polymerization of the network generates a pushing force to open a sufficient wide channel in ECM to drive individual or collective cell migrations (12-14).

Clinical studies show that Arp2/3 complex-medicated migration is tightly associated with cancer invasion (15-20), and patients over expressing Arp2/3 complex have poor survivals in lung (16), breast (17), pancreatic (20), and colorectal cancers (15). In addition, the migrations of immune cells, such as dendritic cells and T cells, in three-dimensional ECMs are also extensively driven by the Arp2/3 complex formed lamellipodial protrusions (6, 7). However, ECMs *in vivo* are highly mechanically heterogeneous (21, 22). Both invasive cancer cells and immune cells need to migrate long distances to establish new tumors (21, 23) and to find killing targets(7, 24), respectively. Experimental studies show that the magnitude of ECM resistance can affect the density of lamellipodial branched actin filaments (1, 5, 11, 25), and the lamellipodial leading-edge velocity exhibits resistance-history dependent (1, 26). In addition, cells predominantly migrate along the path with the least resistance in heterogeneous extracellular microenvironments (HTECMs) (6). All these studies suggested that the leading edge of migratory cells actively mechano-senses variations of ECMs and adapts its migrating behaviour (Fig. 1*A*) (1, 5, 6, 27) in response to complex ECMs. However, the migratory leading edge involves highly dynamic interplays of various proteins, including Arp2/3 complexes, actin monomers, actin filaments, Wiskott-Aldrich syndrome proteins (WASPs), ATP, capping

proteins, leading-edge membrane, integrin-based adhesions and ECMs (5, 10, 11, 28). Due to both the temporal and spatial cross-scale complexities (29) (Fig. 1*A*), live imaging protein behaviours at millisecond and nanometre scales is intrinsically difficult (30). Thus, quantitatively interpreting how these complicated cell-scale self-adaptive migration behaviours (Fig. 1*A*) emerge from the dynamic activities of molecular proteins has been a grand and long-lasting challenge (31, 32). It not only seriously hampers our in-depth mechanistic understandings of *in vivo* cell migrations, but also hinders us from discovering target proteins for designing new medicines and gene editing therapies to prevent cancer cells from invasions or enhance immune cell infiltrations for solid cancer immunotherapy.

Constructing a predictive spatiotemporal multiscale modelling system that can describe cellular dynamic behaviours from the molecular to cellular scales at the intersection of biology, physics, chemistry and computer science will greatly accelerate biomedical advancements (33, 34). From the level of molecular protein-protein interactions, we here derive a spatiotemporal 'resistance-adaptive propulsion' (RAP) theory based on the geometric nonlinear deformation mechanisms of polymerizing actin filaments and the mechano-chemical assembling behaviours of Arp2/3 complexes. The theory describes both spatial and temporal mechanical interactions between the polymerizing branched actin filaments and the bent leading-edge membrane constrained by ECM. On the basis of this RAP theory, we develop a multiscale spatiotemporal modelling system, which encompasses dynamic actin polymerization, capping protein inhabiting actin filament polymerization, nonlinear deformation of actin filaments, actin monomer diffusion, ATP binding on actin monomers and Arp2/3 complex, mechano-chemical assembly of Arp2/3 complex, detachments of molecular linkers, bent leading-edge membrane and HTECMs. It can not only simulate dynamic cell migrations in complex environments but also quantitatively shed light on synchronous interacting and assembling behaviours of multiple proteins. Combining spatiotemporal simulations with experiments tracking actin

dynamics during cell migration, we discovered a resistance-triggered positive feedback mechanism at the protein level for adapting propulsive forces to overcome the heterogeneity in ECM, and a resistance-triggered negative feedback mechanism for adapting cell morphology to circumnavigate regions with high ECM resistance. Strikingly, the combination of the two opposite feedback mechanisms along the broad lamellipodial leading edge shows formidable synergistic effects, empowering cells with both powerful and flexible migratory capabilities to deal with complex ECMs, and meanwhile endowing intracellular ATP resource with an optimal efficiency in fuelling cell migration. These insights explain why it is hard to prevent metastasis by cancer cells once they have acquired invasive ability. By monitoring the assembling behaviours of proteins, we further find that the nature of migration velocity depending on the resistance history of ECM is derived from the temporal hysteresis of adaptive actin cytoskeleton remodeling. In addition, we reveal that directional cell migration is dictated by the competition between the local stiffness of ECMs and the local polymerizing rates of the leading-edge actin cytoskeleton in response to gradients of chemotactic cues. Overall, we establish the first, to our knowledge, spatiotemporal biophysical theory and multiscale modelling system, which can accurately predict self-adaptive cell migrations in complex ECMs from protein behaviours that happen at the milliseconds *in vivo*. Establishing such predictive biophysical theory and spatiotemporal modelling system will allow computer simulations to replace some laboratory experiments to quantitatively test how new drugs and gene editing technologies targeting on proteins affect cell dynamics in the future.

Spatiotemporal self-adaptive propulsion theory and multiscale modelling system

Branched actin network protrusion is an important way that drives cell migrations in ECMs. Through adding actin monomers to the barbed ends, polymerizing branched actin filaments

grow and thus generate pushing force on the leading-edge membrane (5). Before being capped by capping proteins, the growing length of filaments with the polymerizing time t can be expressed as

$$l(t) = \delta \int_{t^{nuc}}^{t^{cap}} \left[\gamma(\Phi) \cdot \psi(D_a) \cdot \mathbf{C}_a \cdot k_P(\mathbf{p}) \cdot k_{on} - k_{off} \right] \mathrm{d}t \quad (1)$$

where δ is the radius of an actin monomer; t^{nuc} and t^{cap} are the nucleation time and the capping time, respectively; $\mathbf{C}_a$ is the local concentration of actin monomers in the cell; $\gamma(\Phi)$ is the consuming factor of actin monomers, introducing the relation that polymerizing rate is proportional to the ratio of the concentration of actin monomers to the density of polymerizing filaments Φ (35); ψ is a scaled diffusion coefficient D_a of actin monomers and is to introduce the effect of actin filament density on the actin diffusion flux towards the polymerizing barbed ends based on the Fick's first law of diffusion; k_{on} and k_{off} are the polymerization and depolymerization rate constants, respectively; $k_P(\mathbf{p})$ is an exponential distribution probability density function $k_P(\mathbf{p}) = 1/\exp^{\lambda p}$ where λ is the parameter of the exponential distribution probability density function and p is the value of the interacting force $\mathbf{p}$. $k_P(\mathbf{p})$ is utilized to introduce a force-dependent probability of actin filament polymerization in each time step. Specifically, when there is a stronger interacting force between the barbed end of actin filaments and the cell membrane, it becomes more challenging for an actin monomer to polymerize at the barbed end (36).

The leading-edge membrane under the polymerizing force of filaments is in a bending state. We simplify it into several continuous inclined planes based on the theory of differential geometry (Supplementary Fig. 2*B*). Though the mechanical interactions between all polymerizing actin filaments and the leading-edge membrane are in three-dimensional space, the interaction between a single polymerizing actin filament and the local membrane can be

described in a two-dimensional deformation plane (Fig. 1*B* and Supplementary Fig. 2*C*). Then, based on the geometric nonlinear deformation theory of continuum mechanics, the spatial and temporal mechanical interactions between the growing (polymerizing) actin filament and the leading-edge membrane are derived as (Fig. 1*B*, Supplementary Methods)

$$\beta(s,t)=\frac{\mathbf{p}}{EI}\int_{s(t)}^{l(t)}[(1-\varepsilon(s,t))\int_{0}^{s(t)}(1-\varepsilon(r,t))\sin\beta(r,t)\,\mathrm{d}\,r]\,\mathrm{d}\,s+\frac{2\kappa(1+\nu)\mathbf{p}\sin\beta(s,t)}{EA}+\theta \qquad (2)$$

where $\beta(s,t)$ is the deformed angle along the actin filament due to the combined effects of bending, axial compression and transverse shear under the polymerizing growth; E, ν, A, I, κ are the Young's modulus, Poisson's ratio, cross-sectional area, the second moment of the cross-sectional area and shape factor of actin filaments, respectively. Using the deformation compatibility condition,

$$\int_{0}^{l(t)}[1-\varepsilon(s,t)]\cos\beta(s,t)\,\mathrm{d}\,s=h(t), \qquad (3)$$

the nonlinear deformation function in Eq. (2) can be solved through iteration. h is the distance from the pointed end of the polymerizing actin filament to the local leading-edge membrane. Then, the interacting force $\mathbf{p}(t)$, the propulsive force $\mathbf{f}_p(\theta,t)$ in cell migration direction, the total deformation energy $U(t)$ and the mean bending curvature $\xi(t)=\dfrac{\beta(0)-\beta(l(t))}{l(t)}$ of the actin filament can all be solved (Supplementary Fig. 4*A*-*F*). The total deformation energy $U(t)$ is expressed as

$$\begin{aligned}U(t)=&\frac{\mathbf{p}^2}{2EI}\int_{0}^{l(t)}\left[\int_{0}^{s(t)}(1-\frac{\mathbf{p}\cos\beta}{EA})\sin\beta ds\right]^2\mathrm{d}\,s+\frac{1}{2}\int_{0}^{l(t)}\frac{(\mathbf{p}\cos\beta)^2}{EA}(1-\frac{\mathbf{p}\cos\beta}{EA})\,\mathrm{d}\,s\\&+\int_{0}^{l(t)}\frac{\kappa(1+\nu)(\mathbf{p}\sin\beta)^2}{EA}(1-\frac{\mathbf{p}\cos\beta}{EA})\,\mathrm{d}\,s\end{aligned} \qquad (4)$$

Our mechanical analysis also shows that convex side surface of the bending actin filament is stretched while the concave side surface is compressed (Fig. 1*C*). Their relative strain $\varepsilon_r = 2r_0\xi$ where r_0 is the radius of actin filament. Experiments (37) show that *in vitro* long actin filaments (~10μm) exhibit large bending deformations under thermal fluctuations, and Arp2/3 complexes prefer to bind onto the convex sides of bending actin filaments. We fit the experimental data of relative branched density P with an inverted sigmoid function $P = 2/(1+e^{0.73\xi})$ (Fig. 1*D*) and analyse it. Strikingly, we have , for the first time, obtained the relative curvature-dependent Arp2/3-actin filament dissociation constant $K_d(\mathbf{p})/K_d^0 = 0.5(1+e^{0.73\xi})$ where $K_d(\mathbf{p})$ and K_d^0 are the dissociation constants in the bending and straight states, respectively (Fig. 1*E* and Supplementary information). The relative $K_d(\mathbf{p})/K_d^0$ shows that the affinity of Arp2/3 complex binding on the convex surface (negative curvature side) of actin filament is higher than the straight surface, which is higher than the concave surface (positive curvature side). This could be explained by the combination of our mechanical analysis and the recent cryo-electron structure of Arp2/3 complex-actin filament junction (38-40) (Fig. 1*C* and Supplementary Fig. 1). There are five actin subunits in mother actin filament that contact with Arp2/3 complex, with many of the contact surfaces in the grooves between these subunits (supplementary Fig. 1*A*) (38-40). ArpC1of Arp2/3 even has a protrusion helix that inserts into actin subdomains for binding (supplementary Fig. 1*B*) (38, 40). During polymerization, actin filaments undergo bending deformations under the constraints of cell membrane and ECM, leading to compressions on their concave sides (Fig. 1*B* and *C*). As a result, some of the binding surfaces in the grooves on the concave side is buried (Fig. 1*C*), inducing the decrease of the binding affinity of Arp2/3. On the contrary, the groove sites on the convex side of the bending actin filaments undergoes stretch (Fig. 1*C*), which facilitates Arp2/3 complex binding and improves Arp2/3 binding affinity. To better show this force-dependent binding affinity, we also calculate the relative dissociation constant

$K_d^1(\mathbf{p})/K_d^2(\mathbf{p})$ where $K_d^1(\mathbf{p})$ and $K_d^2(\mathbf{p})$ are the dissociation constants on the convex and concave surfaces, respectively, demonstrating that the binding affinity on the convex surface is much higher than the concave surface (Fig. 1*F*). Our theoretical analysis has shown that although *in vivo* actin filaments are relatively short (~250nm), their polymerization force still can induce them to generate significant backward bending deformations, which could be verified by the actin retrograde flow phenomenon (41) and the recent measurement that the bending curvature can reach up to 10 μm^{-1} (42). This indicates that the force-dependent Arp2/3 complex-actin filament binding affinity occurs *in vivo*. To incorporate that Arp2/3 complex has a higher binding affinity with the convex surface of actin filaments than with straight surface, we introduce a bending curvature-dependent binding factor $d^{arp}(\xi^{\max})$, which is defined as the space between two adjacent Arp2/3 complex branches along an actin filament, where $\xi^{\max}$ is the biggest bending curvature in the deformation history of the actin filament (Eq. S14). The number of Arp2/3 complexes binding on the *i*th actin filament with polymerization length $l_i(t)$ can be determined as $n_i^{arp} = l_i / d^{arp}(\xi_i^{\max})$. The probabilities that an Arp2/3 complex binding on the convex and concave side of an actin filament are $P(|\xi|)/[P(|\xi|)+P(-|\xi|)]$ and $P(-|\xi|)/[P(|\xi|)+P(-|\xi|)]$, respectively. Thus, the total number of actin filaments $N(t)$ pushing against the leading-edge membrane at time t is

$$N(t) = \sum_{i=1}^{m(t)} n_i^{arp}(\xi_i^{\max}) + m(t), \tag{5}$$

where $m(t)$ is the number of mother filaments. During cell migrations, some filaments are linked to the leading-edge membrane through molecular linkers, such as Ezrin and N-WASPs(12, 43-45), and generate a resultant attachment force $\sum_{k=1}^{\Omega(t)} \mathbf{f}_{a,k}(t)$ to pull back the membrane where $\Omega(t)$ and $\mathbf{f}_a$ are the total number of attaching molecular linkers and attaching

force of each molecular linker, respectively. The total number of tethered filaments $\Omega(t) = \alpha N(t)$, where the parameter α is the percentage of the total number of actin filaments contacting with the leading-edge membrane. In the static state, the leading edge of migrating cells follows the force balance condition (Fig. 1*G*):

$$\sum_{j=1}^{N(t)} \mathbf{f}_{p,j}(\theta_j, t) = \sum_{k=1}^{\Omega(t)} \mathbf{f}_{a,k}(t) + \mathbf{f}_m(t) + \mathbf{f}_{ECM}(t), \tag{6}$$

where $\mathbf{f}_m(t)$ and $\mathbf{f}_{ECM}(t)$ are a backward tension force from the leading-edge membrane and a resistance force from ECM, respectively. The total elastic deformation energy stored in all branched filaments pushing the leading-edge membrane is $\prod(t) = \sum_{j=1}^{N(t)} U_j(\theta_j, t)$. Experiments showed that the motion of branched actin filaments is saltatory with a step size $\Delta\mathbf{S}$ of about 1 − 10nm with time (46, 47) due to the detachment of molecular linkers(13, 43, 48). Actually, in vivo, cell migration involves not only the detachments of molecular linkers from leading-edge membrane(43), but also the local ruptures of some nascent integrin adhesions (49) and extracellular crosslinking matrix networks owing to the propulsive force (21, 50). Since these processes are very complex and also involves different energy barriers, in order to capture the key characteristics of cell migration, we assume that when the resultant propulsive force $\sum_{j=1}^{N(t)} \mathbf{f}_{p,j}(\theta_j, t)$ is larger than the maximum resultant stall force $\sum_{k=1}^{\Omega(t)} \mathbf{f}_{a,k}(t) + \mathbf{f}_m(t) + \mathbf{f}_{ECM}(t)$, some molecular linkers will detach from the leading-edge membrane (43) and thus cell will migrate forward with a leaping step size $\Delta\mathbf{S}$. Then, the position of the leading edge of the cell at time $t+1$ can be expressed by

$$\mathbf{S}(t+1)=\begin{cases}\mathbf{S}(t) & if \sum_{j=1}^{N(t+1)}\mathbf{f}_{p,j}(\theta_j,t+1)\le\sum_{k=1}^{\Omega(t+1)}\mathbf{f}_{a,k}(t+1)+\mathbf{f}_m(t+1)+\mathbf{f}_{ECM}(t+1)\\ \mathbf{S}(t)+\Delta\mathbf{S} & if \sum_{j=1}^{N(t+1)}\mathbf{f}_{p,j}(\theta_j,t+1)>\sum_{k=1}^{\Omega(t+1)}\mathbf{f}_{a,k}(t+1)+\mathbf{f}_m(t+1)+\mathbf{f}_{ECM}(t+1)\end{cases} \quad (7)$$

and the transient average migration velocity $\mathbf{V}$ is $\Delta\mathbf{S}/\Delta t$. Because the present theory is derived from the spatiotemporal mechanical interactions between the polymerizing branched actin filaments and the leading-edge membrane constrained by extracellular resistance, and incorporates the force-dependent assembling behaviours of proteins, we name it spatiotemporal 'resistance-adaptive propulsion' (RAP) model.

To quantitatively shed light on how the assembling behaviours of multiple proteins impact on the dynamics of cell migration, we further develop a multiscale spatiotemporal modelling system by applying the RAP theory and integrating the stochastic behaviours of proteins (Supplementary Methods). This modelling framework systematically encompasses the *in vivo* actin monomer nucleation, actin filament polymerization, capping protein terminating filament polymerization, mechano-chemical nucleation of Arp2/3 complex, ATP binding, bent leading-edge membrane, detachments of molecular linkers, protein gradients caused by chemotactic cues, integrin-based adhesion and heterogeneous ECMs. Using this bottom-up approach, we can span multiple scales in both space and time to investigate cell migration behaviours in complex ECMs, and thus shed light on their dominating biophysical principles from the level of specific proteins.

ECM resistance-triggered positive feedback adapts propulsive force

High extracellular resistance results in denser lamellipodial branched actin filaments during cell migrations(1, 5). To explore quantitatively whether our spatiotemporal RAP theory can reproduce this significant behaviour and reveal its underlying biophysical mechanism, we perform spatiotemporal simulations of cell migrations in both mechanically homogeneous

extracellular microenvironment (HMECM) and HTECM (Fig. 2*A*). we observe that when the resistance $\mathbf{f}_{ECM}$ is 0.5 nN/μm (the normal range is 0.1–2.0 nN/μm of ECM(51)) in the HMECM condition, the density of polymerizing branched actin filaments Φ stably fluctuates in a very narrow range 230–270 /μm (Fig. 2*A*), agreeing well with the experimental data 150–350 /μm (51). However, in the HTECM, when the extracellular resistance $\mathbf{f}_{ECM}$ increases from the low resistance (LR) 0.5 nN/μm to a higher resistance (HR) 1.0 nN/μm, the branched actin density Φ increases by ~35% (320–350 /μm, Fig. 2*A*). After $\mathbf{f}_{ECM}$ returning to the low resistance (RLR) 0.5 nN/μm, the density also decreases to its previous level (Fig. 2*A*). The density of Arp2/3 complex assembling actin cytoskeleton cofluctuates with the resistance (Fig. 2*B*). Strikingly, our model well predicts the experimentally measured correlations between the extracellular resistance and the lamellipodial branched actin filament density during cell migration in refs.(1, 5, 11) (Fig. 2*A*). The architecture of the lamellipodial branched actin network generated in our spatiotemporal simulations is also consistent with the experimental measurements (Fig. 2*C*) (52). In addition, we show that when cells encounter higher resistances, the consumption rate of ATP (Fig. 2*D*) increases to fuel cell migrations. This prediction is also validated by the experimental data (Fig. 2*D*) that mitochondria and ATP levels are higher at the invasive cell leading edge in a stiffer ECM confinement (11) and that cancer cells overproduce ATP to boost their lamellipodia formations and invasions (53).

Next, we analyse the spatiotemporal propulsive force (Fig. 2*E*) and the elastic deformation energy Π stored in the branched filaments (Fig. 2*F*). It is found that both synchronously fluctuate with the density of branched actin filaments. We further quantitatively identify that the adaptation of filament density is to meet the propulsive force and energy demands for overcoming the varying extracellular resistance. To shed light on the more fundamental cross-scale biophysical mechanism of such significant adaptive behaviours in response to ECMs, we

286 then examine the assembly of protein molecules that happens at milliseconds, finding an ECM
287 resistance-triggered positive feedback (Fig. 2*G*). When the resistance $\mathbf{f}_{ECM}$ increases,
288 polymerizing (growing) actin filaments under the ECM confinement will automatically have
289 larger nonlinear bending deformations, which increase the probability that Arp2/3 complex
290 will bind and nucleate daughter actin filaments, and vice versa. Through this mechanism, cells
291 can adapt the density of branched actin network and thus the propulsive force and energy for
292 migrations. More importantly, through the extent of bending deformations, cells can sense the
293 ECM resistance, so a larger resistance induces a larger bending deformation. Thus, from the
294 protein level, we reveal that migrating cells can sensitively sense the immediate variations of
295 ECM resistance through the polymerizing growth of actin filaments, and then accordingly
296 make accurate adaptive responses in filament density, propulsive force and energy through the
297 mechano-triggered Arp2/3 complex-actin filament assembling behaviours (Fig. 2*G*). This
298 mechanism also endows migrating cells with an optimization ability to accurately employ their
299 intracellular proteins and ATP (Fig. 2*A*, *B* and *D*) according to their demands in complex ECMs.

300 **Leading-edge velocity depends on the temporal hysteresis of filament density**
301 **adaptation to varying ECM**

302 We next explore how the leading-edge migration velocity responds to the varying stiffness
303 of the ECMs and how the underlying biophysical mechanisms operate at the level of protein
304 molecules. The spatiotemporal simulations in HTECMs show that when migrating cell
305 encounters an increased extracellular resistance $\mathbf{f}_{ECM}$, its leading-edge migrating velocity $\mathbf{V}$
306 suddenly decreases from 3.3 μm/min to 0.7 μm/min (from stage I to II in the black ellipse in
307 Fig. 2*H*), which is lower than the velocity 1.7–5.2 μm/min in the HMECMs with $\mathbf{f}_{ECM}$ = 0.5
308 nN/μm. However, with the continuing polymerization of branched filaments, the decreased
309 velocity partially recovers. This is owing to the gradual increase in the filament density based

310 on the ECM resistance-triggered positive feedback. Afterwards, we reduce the extracellular
311 resistance from 1 nN/μm to its previous value 0.5 nN/μm for the HTECMs. Strikingly, the
312 leading-edge velocity abruptly increases to a very high value 10.7 μm/min, and then gradually
313 decreases to the previous range 1.7-5.2 μm/min (Fig. 2*H*). The spatiotemporal predictions from
314 stage I to V are validated by the experimental data (Fig. 2*H*) (1, 26). To gain insight into the
315 protein behaviours, we check the evolution of the spatiotemporal remodeling of the growing
316 lamellipodial actin network. Previous studies (26) described this phenomenon as velocity
317 dependence on loading history. Here, we quantitatively show that the nature of the leading-
318 edge velocity variations in the HTEMCs stems from that the adaptation of branched actin
319 filament density is always temporally hysteretic to its triggering reason, i.e., varying ECM
320 resistance (Fig. 2*I*). This is because the generation of daughter filaments and their growths to
321 the leading-edge membrane always cost some time due to actin monomer nucleation, filament
322 polymerization, Arp2/3 activation and assembly (Fig. 2*I*). Although the extracellular resistance
323 $\mathbf{f}_{ECM}$ has increased or decreased, the density, propulsive force and deformation energy of
324 polymerizing actin filaments keep unchanged in this process. Thus, the velocity suddenly
325 decreases because of incapable of overcoming the increased resistance, and increases because
326 of easily overcoming the decreased resistance to release the excess deformation energy,
327 respectively (Fig. 2*E* and *F*). This also indicates that, in HTECMs, there exists no one-to-one
328 correspondence between $\mathbf{V}$-$\mathbf{f}_{ECM}$ that can describe the leading-edge migrating behaviours.
329 However, in HMECMs, the one-to-one $\mathbf{V}$-$\mathbf{f}_{ECM}$ relationship exists.

330 High ECM resistance-triggered negative feedback adapts cell morphology
331 for pathfinding

332 The above study focuses on the low ranges of ECM resistance. However, the leading edge
333 usually faces some local dense collagen regions with high resistances in ECM. Thus, we here

334 investigate migratory pathfinding in this kind of complex ECMs and shed light on its
335 underlying mechanistic operating basis at the protein level. We design an ECM as
336 demonstrated by Fig. 3*A*. The ECM is divided into two stages. In the first stage (from 0 to 110
337 nm), it is mechanically homogeneous and has a resistance $\mathbf{f}_{ECM}$ of 0.5 nN/μm. However, in the
338 second stage (from 110 to 300 nm), its resistance becomes 1.0 nN/μm, and there are two very
339 dense collagen regions with a very high resistance $\mathbf{f}_{ECM}^{right} = \mathbf{f}_{ECM}^{left} = 5$ nN/μm.

340 Spatiotemporal simulations show that, in the first homogeneous mechanical environment,
341 the left, central and right parts of the leading edge migrate forward synchronously with similar
342 velocities (Fig. 3*B*). The density of branched actin filaments is approximately homogeneous
343 (Fig. 3*C*). However, when the cell encounters the two dense collagen ECM regions, it stops
344 moving forward from the left and right sides, and turns to squeeze out from the central region
345 where the resistance is weak (Fig. 3*B*). Unexpectedly, even though the leading edges on the
346 left and right sides have not overcome their local resistances, the increase of the density of actin
347 filaments stops (red ellipse area in Fig. 3*C*). Interestingly, this indicates that when the ECM
348 resistance is very high, the mechanism of resistance-triggered positive feedback no longer work.
349 We perform experiments to validate this spatiotemporal model prediction. We record
350 Human retinal pigment epithelial-1 (RPE1) cells expressing green fluorescent protein linked to
351 a small peptide (Lifeact-GFP) with affinity for actin microfilaments. We image the dynamic
352 cell migration processes in the microchannels with constrictions (Fig. 3*D*), and track the
353 temporal actin intensity when the cell encounters the constriction regions. The experimental
354 results of the temporal variations of leading-edge actin intensity (50% increase, Fig. 3*E*) are
355 consistent with the modelling predictions (70% increase, Fig. 3*C*) when the leading edge
356 encounters a very high ECM resistance. We then check how our spatiotemporal simulations
357 operate at the protein level (Fig. 3*F* and *G*). Migrating cells apply the resistance-triggered
358 positive feedback to adapt filament density and propulsive force to try to overcome the

obstacles until high forces between the leading-edge membrane and actin filaments (Fig. 3*H*) compromise the intercalations of actin monomers with the barbed ends (Fig. 3*F*), which stops the bending deformation of filaments (Fig. 3*I*) and the assembly of Arp2/3 complex (Fig. 3*G*). These results of our simulation are strongly validated by *in vitro* experiments (25). We also find that the porosity of the leading-edge actin network is reduced due to the increased density of actin filaments (Fig. 3*J*). This lowers the diffusion of actin monomers to the free barbed ends, and reduces the polymerization rate at the leading edge (Fig. 3*K*).

Unexpectedly, we find that an ECM resistance-triggered negative adaptation feedback (Fig. 3*L*) coexists with the resistance-triggered positive adaptation feedback (Fig. 2*G*) in migrating cells. While the positive feedback adapts cell propulsive force to overcome ECMs, the negative feedback can adapt cell morphology by stopping actin polymerization to circumnavigate the high resistance regions in ECMs. This behaviour can avoid unnecessary consumptions of intracellular proteins and ATP resources (Fig. 3*F* and *G*), and thus improve cell migration efficiency. The synergy of the two opposite feedbacks allows the leading edge to discriminate whether the local ECM confinement is weak to overcome or strong enough to require circumnavigation with a formidable efficiency. It endows the cell with both powerful and flexible migration capabilities to widely adapt morphologies to the complex ECMs (Fig. 3*M*). This may explain why cancer metastasis is extremely hard to prevent once they acquire invasive ability. In addition, our results reveal that the initiation of cellular morphology adaptations, a prominent characteristic of invasive cancer cells, derives from the leading edge sensing strong barriers and escaping from them.

Directional cell migration is steered by a balanced and competing relation

Cells typically follow the gradients of chemotactic cues to migrate (6). The nucleus of migrating cells acts as a mechanical gauge to make temporary adaptations while choosing a

passable path (6, 54, 55). Given the global migration direction predefined by chemotactic cues, leading edge is much more important in persistently directing cell migration towards the final destination. Our simulations demonstrate that different local stiffness of ECM results in different local densities of branched filaments along the leading edge. Here, we investigate another challenging question of how the complex interplays between the multiple simultaneous factors of extracellular resistance, density heterogeneity of branched actin filaments, and the external diffusible chemotactic stimuli synergistically steer directional cell migration in HTECM. We introduce a gradient diffusion of a localised chemotactic cue sensed by transmembrane receptors (Fig. 4*A*), rendering a gradient distribution of intracellular actin monomers. We design and simulate three cases A–C (Fig. 4*B*), in which local leading edges at the positions of $\mathbf{x}_1$ and $\mathbf{x}_2$ simultaneously drive cell migrations. Based on the experimental observations (6), it is reasonable to hypothesize that the fastest migration direction of local leading edges is the main migration direction of a cell. Our simulations in case A show that the migration distance of the leading edge at the position $\mathbf{x}_2$ are larger than those at the position $\mathbf{x}_1$ (Fig. 4*C*), concluding that when the extracellular mechanical microenvironments are homogeneous, cells more actively migrate toward the site where the local concentration of actin monomers is higher. Since homogeneous ECM induces homogeneous density of branch filaments in the whole leading edge (Fig. 4*D*), a higher local concentration of actin monomers means that sufficient actin monomers can be supplied to the polymerizing barbed ends of the local branched actin filaments. The chemotactic cue determines the local protein concentration to steer directional cell migration. Then, we test case B, in which the left and right sides are designed to have the same local concentrations of actin monomers due to homogeneous distribution of the chemotactic cue, but different extracellular resistances. Cells migrate toward the low resistance $\mathbf{x}_1$ side (Fig. 4*E*), because higher resistance on the right-side results in denser branched actin filaments there (Fig. 4*F*), which deplete action monomers locally and thus slows

polymerization rate at barbed ends. This case highlights that extracellular resistance plays a determining role in directing cell migration. However, the results of case C (Supplementary Fig. 5), in contrary to case B, shows that cells migrate toward the high resistance $\mathbf{x}_2$ side (Fig. 4*G*). Even though the denser polymerizing filaments consume more action monomers on the $\mathbf{x}_2$ side (Fig. 4*H*), the strong chemotactic cue can sustain a high local concentration of actin monomers, which enable branched actin filaments to polymerize at a higher rate than that on the $\mathbf{x}_1$ side. Although here we take actin monomers as an example, local variations in the concentrations of other intracellular proteins, such as Arp2/3 complex, WASPs, FMNL, aprin and profilin, have the same effect on cell migration by enhancing or inhibiting nucleation, branch formation and filament polymerization.

From the distinct results of cases A–C, we find that directional cell migration is not solely steered by either the gradients of intracellular proteins induced by chemotactic cues or the local stiffness of ECMs. It is a balanced competing consequence between the two (Fig. 4*I* and *J*). While strong chemotactic cues improve the local nucleation, branch formation and polymerization rate of actin filaments, stiffer local ECMs result in denser local branched actin filaments, which in turn reduce these rates and slow down cell migration. In addition, through the collaboration of the resistance-triggered positive feedback mechanism and the high resistance-triggered negative feedback mechanism, here our results further indicate that as long as the chemotactic cues are strong enough in sustaining the high gradients of proteins for keeping a high branching and polymerizing rates, the leading edge will drive cells to migrate globally and persistently toward the prescribed final destination by overcoming weak confinements and circumnavigating strong barriers encountered.

Discussions

Although cell migrations have been studied many decades, how cells mechano-sense and make self-adaptive responses to complex ECMs at the protein level still remains elusive. In this study, by analysing the spatiotemporal nonlinear deformation of polymerizing actin filaments and the polymerization force-regulated Arp2/3 complex-actin filament binding interactions, we derive a spatiotemporal 'resistance-adaptive propulsion' (RAP) theory for cell migrations. Then, with the RAP theory, we develop a spatiotemporal multiscale modelling system, which can not only simulate dynamic cell migrations in ECMs, but also shed light on the assembling behaviours of single proteins. Our simulations predict many important spatial and temporal adaptive cell migration behaviours observed experimentally and clinically (Table 1), and reveal their underlying operating mechanisms emerged from proteins behaviours.

We find that it is the polymerization force-regulated actin filament-Arp2/3 complex binding interaction that dominates self-adaptive cell migrations in complex ECMs, through the synergistic effects of positive and negative feedbacks. This binding interaction essentially determines the self-adaptive generation of actin filament density (Supplementary Fig. 6) and the orientations of polymerizing actin filaments relative to the direction of cell migration (Fig. 2*C* and Supplementary Fig. 7). During cell migrations, the polymerization-induced bending state of actin filaments serves as a mechano-sensor of cells and a triggering factor for remodeling the actin network based on Arp2/3 complex behaviors. Our finding is highly consistent with recent studies that show bending force (42) and polymerization force (56) evoke conformational changes of actin filaments and thus affect the binding behaviours of actin-binding proteins. In fact, mechanical force-induced conformational change of proteins is a key regulator of protein-protein interactions (57), thereby regulating physiological and pathophysiological cellular behaviours. In addition, actin filaments in cells can grow longer when they are protected from capping by formins or VASP molecules (58, 59) or when the

concentration of capping proteins is low (5). Our simulation results show that longer actin filaments can improve cell migration velocity (Supplementary Fig. 8*A*), which is also validated by the experimental data that Ena/VASP make actin filaments grow longer and thus promotes cell migration velocity (60). The longer actin filaments contribute to the formation of a denser actin network (Supplementary Fig. 8*B*), and each polymerizing actin filament bears a smaller force. This enables them to not only more easily overcome ECM resistance but also polymerize at a higher rate.

Previous studies indicated that increased extracellular resistance induced denser branched actin filaments in the migration leading edge (1, 5, 25). Here, we identify that the enhanced leading-edge actin filament density is to improve the propulsive force and energy to overcome the resistance. Our results physically interpret why Arp2/3 complex overexpression is tightly associated with cancer cell invasions (15-19), poor patient survival in cancers (61) and high migratory force (62). We indicate that Arp2/3 is a key target protein for developing anti-cancer drugs, especially for patients in the advanced stages of cancer. It should be mentioned that the current simulations are for the conditions that integrin-based adhesions are sufficient for fixing the branched actin network. In the event that the levels of integrin or vinculin are not abundant, it is conceivable that high ECM resistance could trigger a rapid actin retrograde flow (41, 63) based on the positive feedback, resulting in an increased backward movement of the branched actin network and subsequently reducing the velocity of cell protrusion. This represents an additional type of negative feedback mechanism that can arise from excessively high ECM resistance. In addition, while cytoskeletal biopolymers generally possess a viscous property (64, 65), it is worth noting that the viscous behaviors of actin filaments become negligible in the millisecond time range (66). As a result, we neglect this aspect in the analysis.

It should be emphasized that polymerization of Arp2/3 complex-branched actin filament network is the most important way for cells to generate propulsive forces to interact with their

surrounding microenvironments and perform their functions. It participates in phagocytosis of immune responses (67), endocytosis (68), dendritic spine formation of cortical neurons (69), T-cell and cancer cell interactions (70), and promoting of DNA fork repair (71) and chromatin organization (72, 73). All these processes require cells to mechano-sense the surrounding microenvironments and then make adaptive force generation responses. Thus, besides cell migrations, our cross-scale findings and the spatiotemporal multiscale modelling system can also be applied to investigate these dynamic physiological cell activities.

Materials and Methods

Cell culture

Human telomerase-immortalized, retinal-pigmented epithelial cells expressing GFP-LifeAct (CellLight Actin-GFP, BacMam 2.0 from Thermo Fischer Scientific) were grown in a humidified incubator at 37°C and 5% CO_2 in DMEM/F12 supplemented with 10% fetal bovine serum and 1% penicillin-streptomycin. All cell culture products were purchased from GIBCO/Life Technologies. Cell lines were regularly checked for mycoplasma contamination (MycoAlert, Lonza).

Cell fixation and immunostaining

Cells were pre-permeabilized in 0.5% Triton X-100 in cytoskeleton buffer for 15 s for tubulin and then fixed in 0.5% glutaraldehyde (no.00216-30; Polysciences) in cytoskeleton buffer with 0.5% Triton X-100 and 10% sucrose for 15 min at room temperature. Cells were then washed three times with PBS-tween 0.1% and incubated in a quenching agent of 1mg ml-1 sodium borohydride for 10 min at room temperature. After fixation, the cells were washed with PBS-Tween 0.1% and then blocked with 3% bovine serum albumin (BSA) overnight. The

cells were incubated with appropriate dilutions of primary antibodies in PBS containing 3% BSA and 0.1% Tween overnight at 4 °C in a humid chamber. After washing three times with PBS-tween 0.1%, the coverslips were then incubated with appropriate dilutions of secondary antibodies diluted in PBS containing 3% BSA and 0.1% for 1 h at room temperature in a humid chamber. After washing three times with PBS-Tween 0.1%, coverslips were then mounted onto slides using Prolong Gold antifade reagent (no. P36935; Invitrogen). Here, we used rat monoclonal antibodies against α-tubulin (no. ab6160, Abcam) and Alexa Fluor 555 goat anti-rat (1:500, no.A21434; Invitrogen) as secondary antibody. Antibodies were diluted as followed for immunofluorescence: α-tubulin (primary: 1:500) and secondary (1:1000). For actin immunofluorescence, Phalloidin-Atto 488 (49409, Sigma-Aldrich) was used to and diluted as 1:1000 to stabilize actin filaments in cells.

Cell migration under constriction

Micro-channels were prepared as previously described (doi:10.1007/978-1-61779-207-6_28). Briefly, polydimethylsiloxane (PDMS, 10/1 w/w PDMS A / crosslinker B) (GE Silicones) was used to prepare 12 µm wide and 5µm high micro-channels with a constriction of 2 µm. For confined migration in Fig. 3*D*, coverslip and micro-channels were treated by plasma for 1mins and then were stuck together at 70 °C for 10mins. Before cell seeding, the microchannels were treated with fibronectin at 10 µg ml-1 for 30mins and incubate with culture medium for 3 hrs at room temperature. GFP-LifeAct RPE1 cells were then seeded in the microchannels with a concentration at 2x105 cells ml-1. Imaging was performed after the overnight incubation of the microchannels.

Imaging

Images of the immunostainings were acquired on a Zeiss LSM900 confocal microscopes (Axio Observer) using a 63x magnification objective (Plan- Apochromat 63X/1.4 oil). Image

acquisition for time-lapse of GFP life-act RPE1 cells in constrictions was performed on a confocal spinning-disc system (EclipseTi-E Nikon inverted microscope equipped with a CSUX1-A1 Yokogawa confocal head, an Evolve EMCCD camera from Roper Scientific, Princeton Instruments) through an 63x magnification objective (Nikon CFI Plan Fluor 60X/0.7 oil) objective every 4 s during 2 hrs for each time-lapse. The set-up was equipped with a live cell chamber, and the temperature was constantly kept at 37 °C. Labelled-actin was excited with a 491 nm laser line, and emission was observed with a standard GFP filter. The microscope was monitored with MetaMorph software (Universal Imaging).

Spatiotemporal theoretical model and dynamic multiscale modelling system

The derivation of the spatiotemporal biophysical theory and the developing process of the spatiotemporal multiscale dynamic modelling system are provided in the Supplementary Text.

Data availability

The data that support the findings of this study are available from the corresponding author on reasonable request.

Author contributions

X.D.C., X.Q.F., H.X.Z. and M.G. designed the research. X.D.C., H.X.Z. and X.Q.F. developed the theory and the spatiotemporal simulation framework. X.D.C performed the simulations. X.D.C., B.W.X. and Y.H.M analysed the data. X.D.C. and Y.H.L. did the experiments and analysed experimental data. X.D.C., X.Q.F., H.X.Z., Y.H.L. and M.G. wrote the manuscript.

Acknowledgements

We gratefully thank Professor Thomas D. Pollard for his invaluable insights and great help for manuscript preparation, and Professor Laurent Blanchoin for help with the experiments. We also thank Professors Xin Liang, Congying Wu, Bo Li and Yue Shao for valuable discussions. X.D.C., X.Q.F, and B.W.X. acknowledge the support from the National Natural Science Foundation of China (Grant no. 11921002 and 12032014)

Competing interests

The authors declare no conflict of interest.

Code availability

All computer codes are available from the corresponding authors on reasonable request.

References

1. Mueller J, *et al.* (2017) Load adaptation of lamellipodial actin networks. *Cell* 171(1):188-200. e116.
2. Bera K, *et al.* (2022) Extracellular fluid viscosity enhances cell migration and cancer dissemination. *Nature*:1-9.
3. Chen X, *et al.* (2020) Predictive assembling model reveals the self-adaptive elastic properties of lamellipodial actin networks for cell migration. *Communications biology* 3(1):1-17.
4. Chan CE & Odde DJ (2008) Traction dynamics of filopodia on compliant substrates. *Science* 322(5908):1687-1691.
5. Bieling P, *et al.* (2016) Force Feedback Controls Motor Activity and Mechanical Properties of Self-Assembling Branched Actin Networks. *Cell* 164(1-2):115-127.
6. Renkawitz J, *et al.* (2019) Nuclear positioning facilitates amoeboid migration along the path of least resistance. *Nature* 568(7753):546.

7. Liu T-l, *et al.* (2018) Observing the cell in its native state: Imaging subcellular dynamics in multicellular organisms. *Science* 360(6386):eaaq1392.
8. Chen B-C, *et al.* (2014) Lattice light-sheet microscopy: imaging molecules to embryos at high spatiotemporal resolution. *Science* 346(6208).
9. Svitkina TM & Borisy GG (1999) Arp2/3 complex and actin depolymerizing factor/cofilin in dendritic organization and treadmilling of actin filament array in lamellipodia. *The Journal of cell biology* 145(5):1009-1026.
10. Blanchoin L, *et al.* (2000) Direct observation of dendritic actin filament networks nucleated by Arp2/3 complex and WASP/Scar proteins. *Nature* 404(6781):1007.
11. Kelley LC, *et al.* (2019) Adaptive F-actin polymerization and localized ATP production drive basement membrane invasion in the absence of MMPs. *Developmental cell* 48(3):313-328. e318.
12. Mehidi A, *et al.* (2021) Forces generated by lamellipodial actin filament elongation regulate the WAVE complex during cell migration. *Nature Cell Biology*:1-15.
13. Mogilner A & Oster G (2003) Force generation by actin polymerization II: the elastic ratchet and tethered filaments. *Biophysical journal* 84(3):1591-1605.
14. Lin Y (2009) Mechanics model for actin-based motility. *Physical Review E* 79(2):021916.
15. Frentzas S, *et al.* (2016) Vessel co-option mediates resistance to anti-angiogenic therapy in liver metastases. *Nature medicine* 22(11):1294-1302.
16. Semba S, *et al.* (2006) Coexpression of actin-related protein 2 and Wiskott-Aldrich syndrome family verproline-homologous protein 2 in adenocarcinoma of the lung. *Clinical cancer research* 12(8):2449-2454.
17. Kazazian K, *et al.* (2017) Plk4 promotes cancer invasion and metastasis through Arp2/3 complex regulation of the actin cytoskeleton. *Cancer research* 77(2):434-447.
18. Molinie N & Gautreau A (2017) The Arp2/3 regulatory system and its deregulation in cancer. *Physiological reviews* 98(1):215-238.
19. Zhao K, *et al.* (2020) WDR63 inhibits Arp2/3-dependent actin polymerization and mediates the function of p53 in suppressing metastasis. *EMBO reports* 21(4):e49269.
20. Juin A, *et al.* (2019) N-WASP Control of LPAR1 Trafficking Establishes Response to Self-Generated LPA Gradients to Promote Pancreatic Cancer Cell Metastasis. *Dev Cell* 51(4):431-445 e437.

21. Wisdom KM, *et al.* (2018) Matrix mechanical plasticity regulates cancer cell migration through confining microenvironments. *Nature communications* 9(1):4144.
22. Park D, *et al.* (2019) Extracellular matrix anisotropy is determined by TFAP2C-dependent regulation of cell collisions. *Nature Materials*:1-12.
23. Di Martino JS, *et al.* (2021) A tumor-derived type III collagen-rich ECM niche regulates tumor cell dormancy. *Nature Cancer*:1-18.
24. Rafiq S, Hackett CS, & Brentjens RJ (2020) Engineering strategies to overcome the current roadblocks in CAR T cell therapy. *Nature reviews Clinical oncology* 17(3):147-167.
25. Bieling P, Weichsel J, Mullins RD, & Fletcher DA (2022) The molecular mechanism of load adaptation by branched actin networks. *Elife* 11:e73145.
26. Parekh SH, Chaudhuri O, Theriot JA, & Fletcher DA (2005) Loading history determines the velocity of actin-network growth. *Nature cell biology* 7(12):1219.
27. Boujemaa-Paterski R, *et al.* (2017) Network heterogeneity regulates steering in actin-based motility. *Nature communications* 8(1):655.
28. Simon C, *et al.* (2019) Actin dynamics drive cell-like membrane deformation. *Nature Physics*:1.
29. Qin Y, *et al.* (2021) A multi-scale map of cell structure fusing protein images and interactions. *Nature*:1-7.
30. Li D, *et al.* (2015) Extended-resolution structured illumination imaging of endocytic and cytoskeletal dynamics. *Science* 349(6251).
31. Stuelten CH, Parent CA, & Montell DJ (2018) Cell motility in cancer invasion and metastasis: insights from simple model organisms. *Nature reviews Cancer* 18(5):296.
32. Mogilner A (2006) On the edge: modeling protrusion. *Current opinion in cell biology* 18(1):32-39.
33. Singla J, *et al.* (2018) Opportunities and Challenges in Building a Spatiotemporal Multi-scale Model of the Human Pancreatic β Cell. *Cell* 173(1):11-19.
34. Sun S-Y, *et al.* (2022) Bio-chemo-mechanical coupling models of soft biological materials: A review. *Advances in Applied Mechanics* 55:309.
35. Lee CW, *et al.* (2013) Dynamic localization of G-actin during membrane protrusion in neuronal motility. *Current Biology* 23(12):1046-1056.
36. Mogilner A & Oster G (1996) Cell motility driven by actin polymerization. *Biophysical journal* 71(6):3030-3045.

37. Risca VI, *et al.* (2012) Actin filament curvature biases branching direction. *Proceedings of the National Academy of Sciences* 109(8):2913-2918.
38. Fäßler F, Dimchev G, Hodirnau V-V, Wan W, & Schur FKM (2020) Cryo-electron tomography structure of Arp2/3 complex in cells reveals new insights into the branch junction. *Nature Communications* 11(1):6437.
39. Chou SZ, Chatterjee M, & Pollard TD (2022) Mechanism of actin filament branch formation by Arp2/3 complex revealed by a high-resolution cryo-EM structureof the branch junction. *Proceedings of the National Academy of Sciences* 119(49):e2206722119.
40. Ding B, *et al.* (2022) Structure of Arp2/3 complex at a branched actin filament junction resolved by single-particle cryo-electron microscopy. *Proceedings of the National Academy of Sciences* 119(22):e2202723119.
41. Bangasser BL, *et al.* (2017) Shifting the optimal stiffness for cell migration. *Nature communications* 8(1):15313.
42. Reynolds MJ, Hachicho C, Carl AG, Gong R, & Alushin GM (2022) Bending forces and nucleotide state jointly regulate F-actin structure. *Nature* 611(7935):380-386.
43. Welf ES, *et al.* (2020) Actin-membrane release initiates cell protrusions. *Developmental Cell*.
44. Senju Y, *et al.* (2017) Mechanistic principles underlying regulation of the actin cytoskeleton by phosphoinositides. *Proceedings of the National Academy of Sciences* 114(43):E8977-E8986.
45. Co C, Wong DT, Gierke S, Chang V, & Taunton J (2007) Mechanism of actin network attachment to moving membranes: barbed end capture by N-WASP WH2 domains. *Cell* 128(5):901-913.
46. Shaevitz JW & Fletcher DA (2007) Load fluctuations drive actin network growth. *Proceedings of the National Academy of Sciences* 104(40):15688-15692.
47. Kuo SC & McGrath JL (2000) Steps and fluctuations of Listeria monocytogenes during actin-based motility. *Nature* 407(6807):1026.
48. Alberts JB & Odell GM (2004) In silico reconstitution of Listeria propulsion exhibits nano-saltation. *PLoS biology* 2(12):e412.
49. Thoumine O, Kocian P, Kottelat A, & Meister J-J (2000) Short-term binding of fibroblasts to fibronectin: optical tweezers experiments and probabilistic analysis. *European Biophysics Journal* 29(6):398-408.

50. Adebowale K, *et al.* (2021) Enhanced substrate stress relaxation promotes filopodia-mediated cell migration. *Nature Materials*:1-10.
51. Abraham VC, Krishnamurthi V, Taylor DL, & Lanni F (1999) The actin-based nanomachine at the leading edge of migrating cells. *Biophysical journal* 77(3):1721-1732.
52. Maly IV & Borisy GG (2001) Self-organization of a propulsive actin network as an evolutionary process. *Proceedings of the National Academy of Sciences* 98(20):11324-11329.
53. Delaunay S, *et al.* (2022) Mitochondrial RNA modifications shape metabolic plasticity in metastasis. *Nature*:1-11.
54. Lomakin A, *et al.* (2020) The nucleus acts as a ruler tailoring cell responses to spatial constraints. *Science* 370(6514).
55. Venturini V, *et al.* (2020) The nucleus measures shape changes for cellular proprioception to control dynamic cell behavior. *Science* 370(6514).
56. Oosterheert W, Klink BU, Belyy A, Pospich S, & Raunser S (2022) Structural basis of actin filament assembly and aging. *Nature*:1-6.
57. Wang Y, *et al.* (2021) Force-dependent interactions between talin and full-length vinculin. *Journal of the American Chemical Society* 143(36):14726-14737.
58. Mullins RD, Bieling P, & Fletcher DA (2018) From solution to surface to filament: actin flux into branched networks. *Biophysical reviews* 10(6):1537-1551.
59. Funk J, *et al.* (2021) A barbed end interference mechanism reveals how capping protein promotes nucleation in branched actin networks. *Nature communications* 12(1):1-17.
60. Bear JE, *et al.* (2002) Antagonism between Ena/VASP proteins and actin filament capping regulates fibroblast motility. *Cell* 109(4):509-521.
61. Broutier L, *et al.* (2017) Human primary liver cancer–derived organoid cultures for disease modeling and drug screening. *Nature medicine* 23(12):1424-1435.
62. Krndija D, *et al.* (2019) Active cell migration is critical for steady-state epithelial turnover in the gut. *Science* 365(6454):705-710.
63. Isomursu A, *et al.* (2022) Directed cell migration towards softer environments. *Nature Materials* 21(9):1081-1090.
64. Hu J, *et al.* (2019) High stretchability, strength, and toughness of living cells enabled by hyperelastic vimentin intermediate filaments. *Proceedings of the national Academy of Sciences* 116(35):17175-17180.

65. Hang J-T, Xu G-K, & Gao H (2022) Frequency-dependent transition in power-law rheological behavior of living cells. *Science Advances* 8(18):eabn6093.
66. Kojima H, Ishijima A, & Yanagida T (1994) Direct measurement of stiffness of single actin filaments with and without tropomyosin by in vitro nanomanipulation. *Proceedings of the National Academy of Sciences* 91(26):12962-12966.
67. Jaumouillé V, Cartagena-Rivera AX, & Waterman CM (2019) Coupling of β2 integrins to actin by a mechanosensitive molecular clutch drives complement receptor-mediated phagocytosis. *Nature cell biology* 21(11):1357-1369.
68. Yang C*, et al.* (2022) Actin polymerization promotes invagination of flat clathrin-coated lattices in mammalian cells by pushing at lattice edges. *Nature communications* 13(1):1-20.
69. Kim IH*, et al.* (2015) Spine pruning drives antipsychotic-sensitive locomotion via circuit control of striatal dopamine. *Nature neuroscience* 18(6):883.
70. Basu R*, et al.* (2016) Cytotoxic T cells use mechanical force to potentiate target cell killing. *Cell* 165(1):100-110.
71. Lamm N*, et al.* (2020) Nuclear F-actin counteracts nuclear deformation and promotes fork repair during replication stress. *Nature Cell Biology* 22(12):1460-1470.
72. Schrank BR*, et al.* (2018) Nuclear ARP2/3 drives DNA break clustering for homology-directed repair. *Nature* 559(7712):61-66.
73. Debaugnies M*, et al.* (2023) RHOJ controls EMT-associated resistance to chemotherapy. *Nature*:1-8.

Figures 1－4

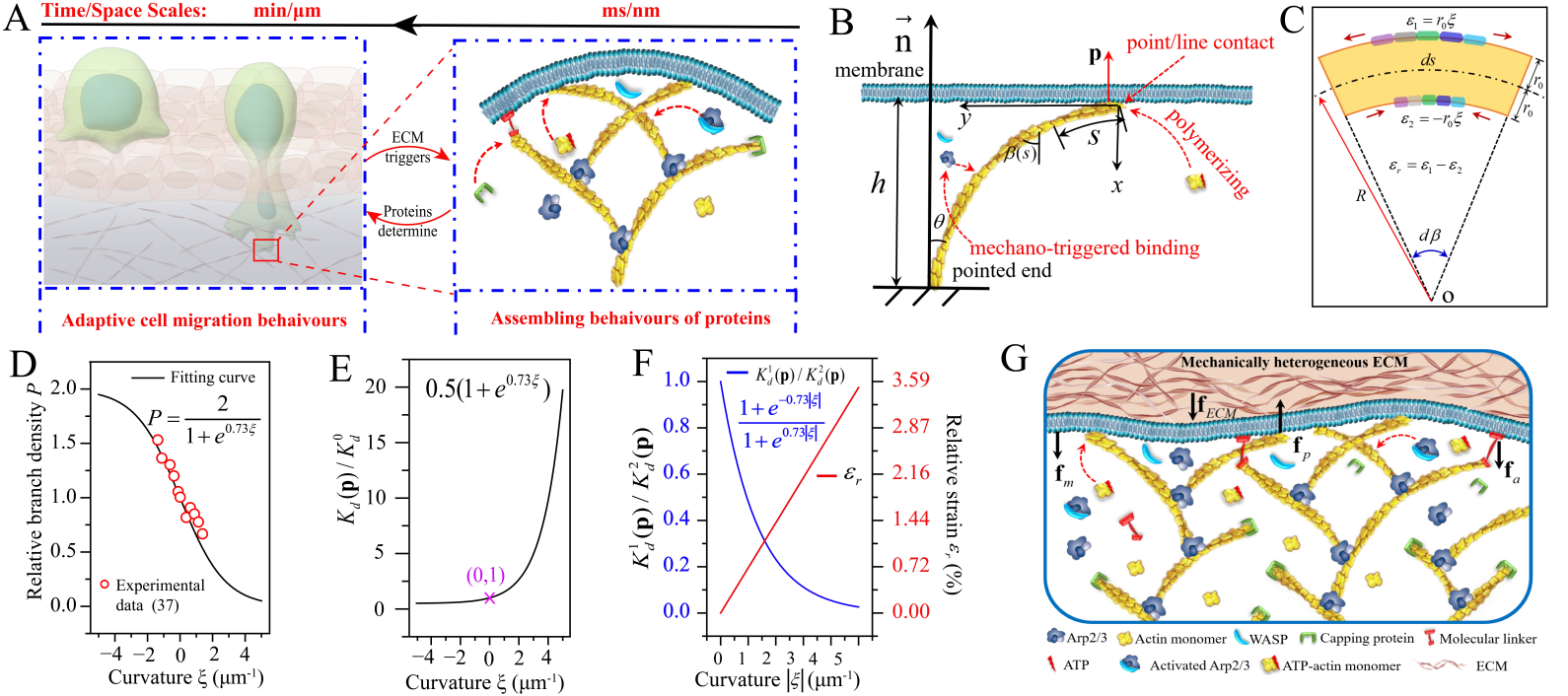
A
Time/Space Scales: min/μm ms/nm
ECM triggers
Proteins determine
Adaptive cell migration behaivours
Assembling behaivours of proteins
B
membrane
point/line contact
polymerizing
mechano-triggered binding
pointed end
C
D
Fitting curve
Experimental data (37)
Relative branch density P
Curvature ξ (μm-1)
E
(0,1)
Curvature ξ (μm-1)
F
Relative strain εr (%)
Curvature |ξ| (μm-1)
G
Mechanically heterogeneous ECM
Arp2/3
Actin monomer
WASP
Capping protein
Molecular linker
ATP
Activated Arp2/3
ATP-actin monomer
ECM

732 **Fig. 1.** Polymerizing branched actin filaments at lamellipodial leading edge drive cells
733 to migrate in ECMs. (*A*) Cell migrations in ECMs are spatial and temporal cross-scale
734 biophysical behaviours performed by proteins. (*B*) Demonstration of the two-
735 dimensional mechanical interaction for theoretical analysis. (*C*) Polymerization-induced
736 deformation analysis of a small segment ds of actin filament. The convex side surface
737 is stretched with a strain $\varepsilon_1 = r_0\xi$ while the concave side surface is compressed with a
738 strain $\varepsilon_2 = -r_0\xi$ where r_0 is the radius of actin filaments. The colour bar regions denote
739 the binding surfaces of Arp2/3 complex on the convex and concave sides of the actin
740 filaments. (*D*) Relationship between relative branched density and actin filament
741 curvature from experimental data (37). It is fitted by an inverted sigmoid function, which
742 is more reasonable than a linear fitting because the relative branched density should be
743 neither minus nor excessively high. The relative branched density P is the ratio of the
744 number of branch points with different curvatures to the corresponding number of mother
745 actin filaments. (*E*) Relationship between the relative dissociation constants $K_d(\mathbf{p})/K_d^0$
746 and actin filament curvature where $K_d(\mathbf{p})$ and K_d^0 are the dissociation constants in the
747 bending and straight states, respectively (Supplementary information). (*F*) The relative
748 dissociation constants $K_d^1(\mathbf{p})/K_d^2(\mathbf{p})$ shows that the binding affinity of Arp2/3 complex
749 on the convex side ($K_d^1(\mathbf{p})$) of a bending actin filament is much higher than the concave
750 surface ($K_d^2(\mathbf{p})$). (*G*) Forces acting on the leading-edge membrane when a cell is
751 migrating in ECMs. $\mathbf{f}_p$ is the propulsive force generated by the polymerization of a
752 branched actin filament. $\mathbf{f}_{ECM}$ is the extracellular resistance from the ECM. $\mathbf{f}_m$ is the
753 tension force of the top and bottom lamellipodial membrane. $\mathbf{f}_a$ is the attachment force
754 of a molecular linker, which links actin filament and the leading-edge membrane.

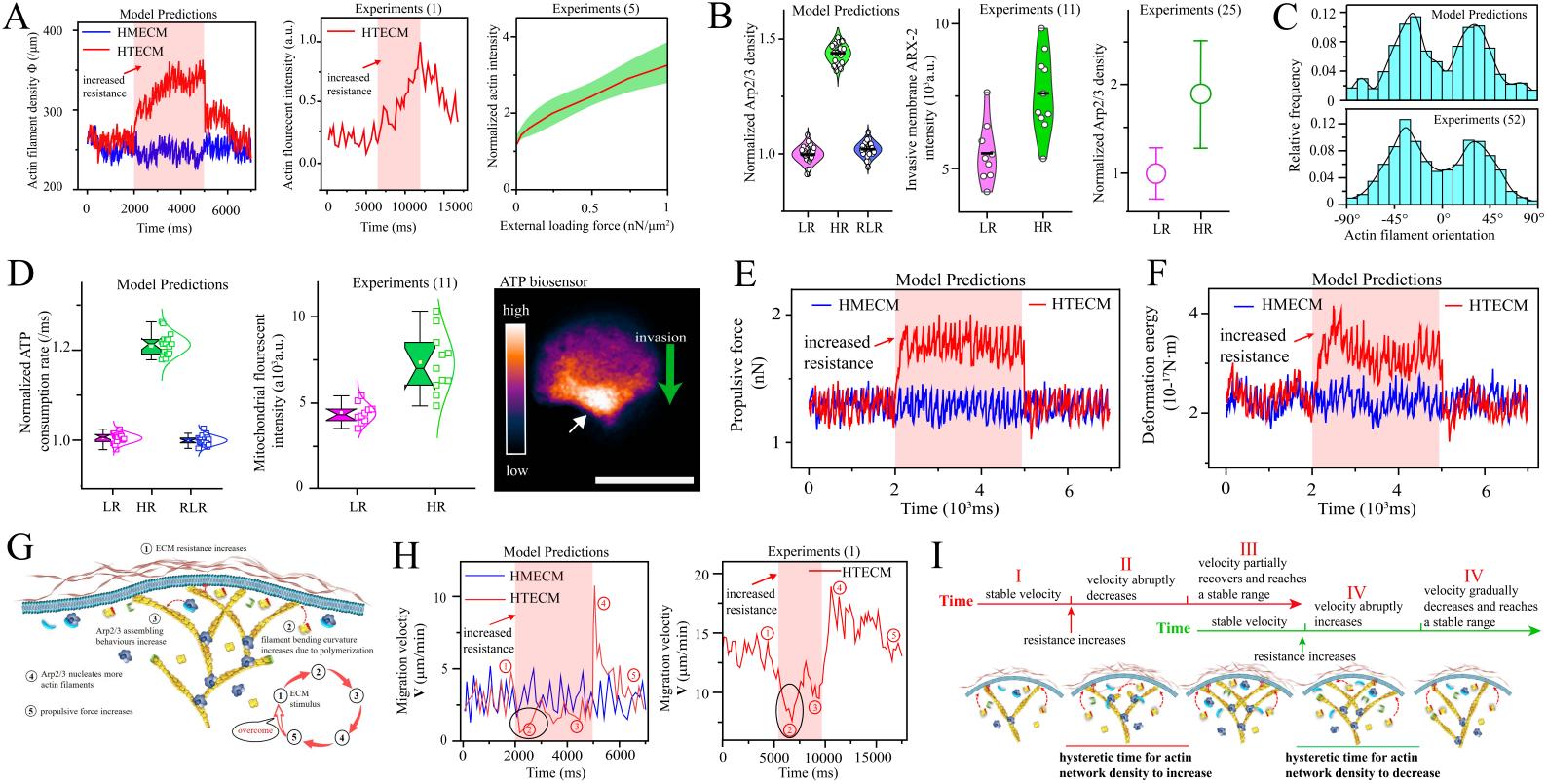
A
Model Predictions
HMECM
HTECM
increased resistance
Actin filament density Φ (/μm)
Time (ms)
Experiments (1)
HTECM
increased resistance
Actin flourecent intensity (a.u.)
Time (ms)
Experiments (5)
Normalized actin intensity
External loading force (nN/μm²)
B
Model Predictions
Normalized Arp2/3 density
LR HR RLR
Experiments (11)
Invasive membrane ARX-2 intensity (10³a.u.)
LR HR
Experiments (25)
Normalized Arp2/3 density
LR HR
C
Model Predictions
Experiments (52)
Relative frequency
-90° -45° 0° 45° 90°
Actin filament orientation
D
Model Predictions
Normalized ATP consumption rate (/ms)
LR HR RLR
Experiments (11)
Mitochondrial flourescent intensity (a.u.)
LR HR
ATP biosensor
high
low
invasion
E
Model Predictions
HMECM
HTECM
increased resistance
Propulsive force (nN)
Time (10³ms)
F
Model Predictions
HMECM
HTECM
increased resistance
Deformation energy (10⁻¹⁷N·m)
Time (10³ms)
G
① ECM resistance increases
② filament bending curvature increases due to polymerization
③ Arp2/3 assembling behaviours increase
④ Arp2/3 nucleates more actin filaments
⑤ propulsive force increases
ECM stimulus
overcome
H
Model Predictions
HMECM
HTECM
increased resistance
Migration velocity V (μm/min)
Time (ms)
Experiments (1)
HTECM
increased resistance
Migration velocity V (μm/min)
Time (ms)
I
Time
I stable velocity
II velocity abruptly decreases
III velocity partially recovers and reaches a stable range
IV velocity abruptly increases
IV velocity gradually decreases and reaches a stable range
resistance increases
hysteretic time for actin network density to increase
hysteretic time for actin network density to decrease

Fig. 2. Spatiotemporal simulations from protein behaviours accurately predict self-adaptive cell migrations in complex ECMs and reveal their underlying biophysical mechanisms. (*A*) Resistance force-induced branched actin network density adaption. Model predictions: temporal fluctuations of polymerizing actin cytoskeletal density at the leading edge in HMECM (blue line) and HTECM (red line). The extracellular resistance $\mathbf{f}_{ECM}$ of the HMECM is 0.5 nN/μm. For the HTECM condition (red line), the $\mathbf{f}_{ECM}$ is 1.0nN/μm in the time frame 2000–5000 ms (shadow region), and is 0.5 nN/μm in the time frames of 0–2000 ms and 5000–7000 ms. The induced actin density along the leading edge in the two conditions is 200–350 /μm, agreeing well with the experimental data 150–350 /μm(51). The first experimental data is the temporal fluctuations of actin reporter lifeact: GFP intensity at the leading edge of migrating fish keratocytes in HTECMs from experiments in ref. (1). The second experimental data is the fluctuations of polymerizing branched actin density in responding to varying external loads from experiments in ref.(5). Actin density is normalized by that of the unloaded condition(5). Green region is the standard deviation. (*B*) Resistance force-induced Arp2/3 complex density adaption. Model predictions: temporal fluctuations of the leading-edge Arp2/3 density in responding to HTECMs (n=30 each group). The Arp2/3 density is normalized by that of the homogeneous ECM condition. The first experimental data: adaptive fluorescent intensity of ARX-2::GFP for Arp2/3 complex at the leading edge when cells invade ECMs with low resistance and high resistance (n=10 each group) from experiments in ref. (11). The second experimental data: Arp2/3 complex density under increasing resistance (n=15 each group) from experiments in ref. (25). The HR condition is normalized by the LR condition. (*C*) Model predictions and published experimental measurements(52) of the orientation frequency of lamellipodial actin filaments relative to the migration direction, which is defined as 0° direction. (*D*) Adaptive ATP

consumption rate for fuelling cells migrating through HTECMs. Model predictions: the ATP consumption rate is the average number of ATP used for assembling actin cytoskeleton per micro-second, and is normalized by that of the HMECM condition (n=20 each group). Experiments: adaptive fluorescent intensity of mitochondria and ATP at the leading edge when cells invade ECMs with low resistance and high resistance (n=10 each group) from ref. (11). Scale bar is 5 μm. Temporal fluctuations of propulsive force (*E*) and deformation energy (F) generated by the leading-edge actin cytoskeleton in HMECM and HTECM. (*G*) Molecular protein-level biophysical mechanism of the positive feedback that migrating cells mechano-sense the variation of ECM and then accurately adapt their propulsive forces to overcome it. (*H*) Velocity adaptation. Model predictions: temporal fluctuations of leading-edge migration velocities in HMECM and HTECM. Experiments: temporal fluctuations of leading-edge migration velocity in responding to HTECM from the experiments in ref.(1). (*I*) Molecular biophysical mechanism of leading-edge migration velocity depending on extracellular resistance history is the temporal hysteresis of the leading-edge actin cytoskeleton remodeling and adaptation. The red and green time lines correspond to the velocity adaptations caused by the increased and decreased ECM resistances, respectively. Velocity adaptation stages I–V in (*I*) correspond to the stages ①–⑤ in (*H*), respectively.

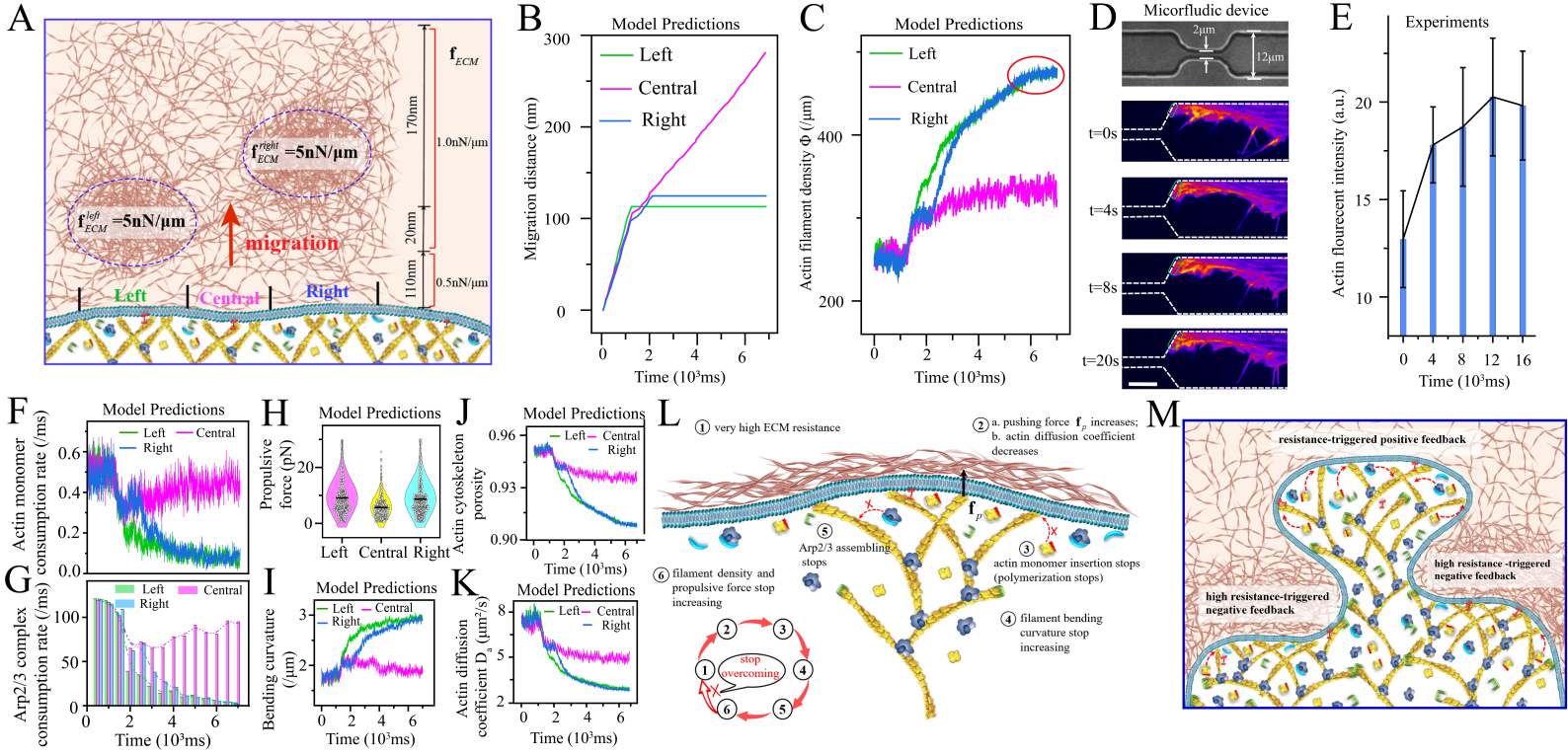
A
f_{ECM}
170nm
1.0nN/μm
20nm
110nm
0.5nN/μm
f_{ECM}^{right} =5nN/μm
f_{ECM}^{left} =5nN/μm
migration
Left
Central
Right
B
Model Predictions
Left
Central
Right
Migration distance (nm)
Time (10^3ms)
C
Model Predictions
Left
Central
Right
Actin filament density Φ (/μm)
Time (10^3ms)
D
Micorfludic device
2μm
12μm
t=0s
t=4s
t=8s
t=20s
E
Experiments
Actin flourecent intensity (a.u.)
Time (10^3ms)
F
Model Predictions
Left
Central
Right
Actin monomer consumption rate (/ms)
G
Left
Central
Right
Arp2/3 complex consumption rate (/ms)
Time (10^3ms)
H
Model Predictions
Propulsive force (pN)
Left
Central
Right
I
Model Predictions
Left
Central
Right
Bending curvature (/μm)
Time (10^3ms)
J
Model Predictions
Left
Central
Right
Actin cytoskeleton porosity
Time (10^3ms)
K
Model Predictions
Left
Central
Right
Actin diffusion coefficient D_a (μm²/s)
Time (10^3ms)
L
① very high ECM resistance
② a. pushing force f_p increases;
b. actin diffusion coefficient decreases
③ actin monomer insertion stops (polymerization stops)
④ filament bending curvature stop increasing
⑤ Arp2/3 assembling stops
⑥ filament density and propulsive force stop increasing
stop overcoming
M
resistance-triggered positive feedback
high resistance -triggered negative feedback
high resistance-triggered negative feedback

800 **Fig. 3.** High extracellular resistance triggers negative feedback to adapt cell morphology
801 to circumnavigate obstacles for compromisingly pathfinding. (*A*) The designed HTECM
802 in simulations. It is divided into two stages, where extracellular resistances in the first (in
803 the range of 0–110 nm in front of the migrating cell leading edge) and second stages (in
804 the range of 110–300 nm in front of the migrating cell leading edge) are 0.5 nN/μm and
805 1.0 nN/μm, respectively. However, the second stage has two dense ECM regions with a
806 very high resistance $\mathbf{f}_{ECM}^{left} = \mathbf{f}_{ECM}^{right} = 5$ nN/μm. The red arrow denotes cell migration
807 direction. Spatiotemporal migration distances (*B*) and leading-edge actin filament
808 densities (*C*) at the left, central and right parts of the leading edge. (*D* and *E*) Microfluidic
809 device and temporal fluctuation of actin reporter GFP-lifeact: the actin intensity as a
810 function of the time at the leading edge when migrating cells encounter an obstacle (n=10
811 each group). Scale bar in (*D*) is 5 μm. Temporal actin monomer (*F*) and Arp2/3 complex
812 (*G*) consumption rates at the left, central and right local leading edges. Actin monomer
813 consumption rate is the ratio of the number of actin monomers adding to the barbed ends
814 of actin filaments to the number of uncapped actin filaments per micro-second. Arp2/3
815 complex consumption rate is the number of Arp2/3 complex assembling for the actin
816 cytoskeleton in a time span of 500 ms. (*H*) Propulsive forces produced by each
817 polymerizing actin filaments at the left, central and right local leading edges. Temporal
818 fluctuations of the average bending curvature of polymerizing actin filaments(*I*), the
819 leading-edge actin cytoskeleton porosity (*J*) and the actin diffusion coefficient (*K*). (*L*)
820 Biophysical mechanism of the high ECM resistance-triggered negative adaptation
821 feedback. (*M*) Demonstration of simulation results that the leading edge circumnavigates
822 high ECM resistance regions based on the negative feedback and opens a channel in the
823 weak region based on the positive feedback. The positive and negative feedbacks work
824 cooperatively to adapt cell morphology and drive cell migration.

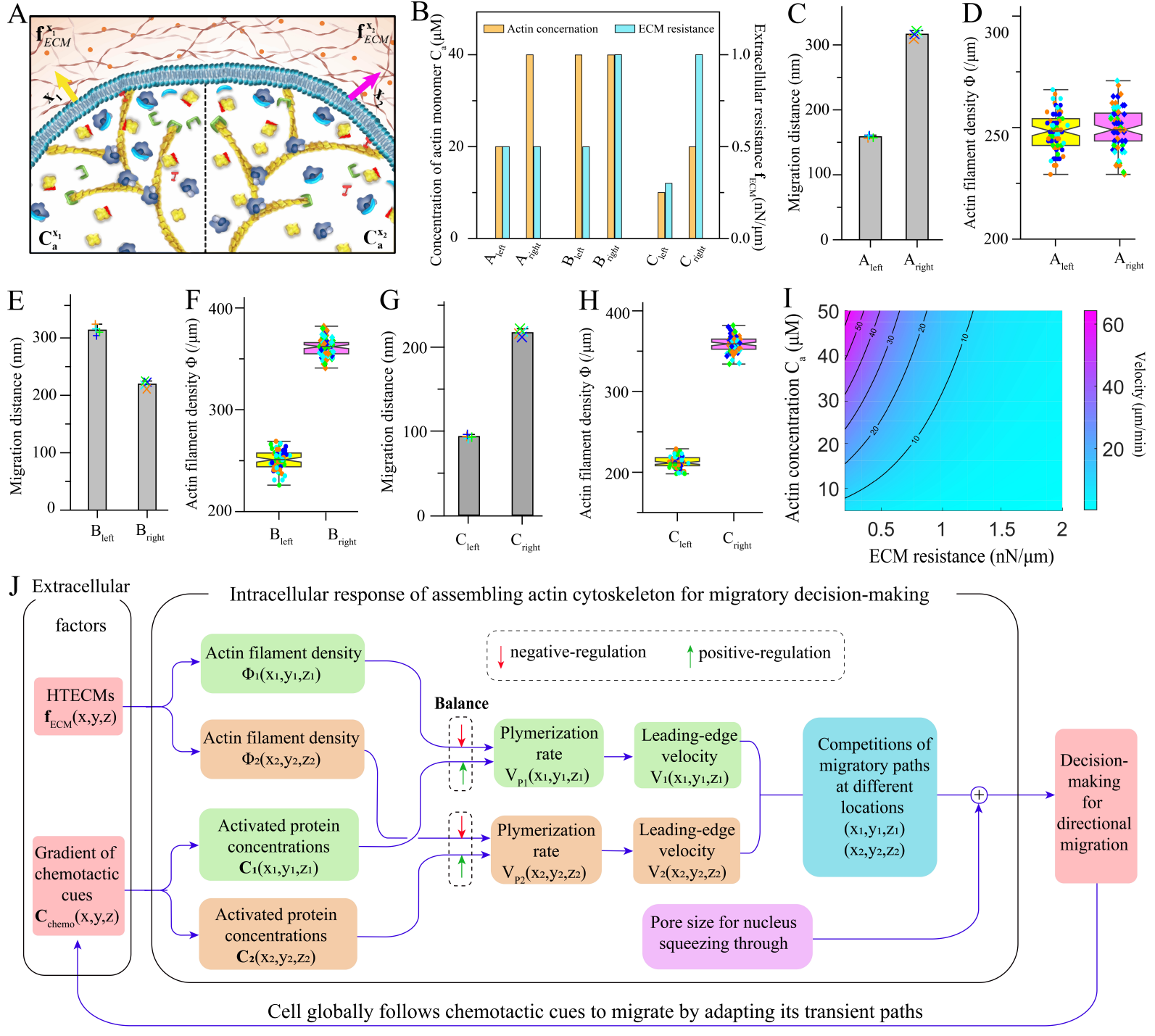
A
B
C
D
E
F
G
H
I
J
Actin concernation
ECM resistance
Concentration of actin monomer C_a (μM)
Extracellular resistance f_{ECM} (nN/μm)
Migration distance (nm)
Actin filament density Φ (/μm)
Actin concentration C_a (μM)
ECM resistance (nN/μm)
Velocity (μm/min)
Extracellular factors
Intracellular response of assembling actin cytoskeleton for migratory decision-making
HTECMs $f_{ECM}(x,y,z)$
Gradient of chemotactic cues $C_{chemo}(x,y,z)$
Actin filament density $\Phi_1(x_1,y_1,z_1)$
Actin filament density $\Phi_2(x_2,y_2,z_2)$
Activated protein concentrations $C_1(x_1,y_1,z_1)$
Activated protein concentrations $C_2(x_2,y_2,z_2)$
negative-regulation
positive-regulation
Balance
Plymerization rate $V_{p1}(x_1,y_1,z_1)$
Plymerization rate $V_{p2}(x_2,y_2,z_2)$
Leading-edge velocity $V_1(x_1,y_1,z_1)$
Leading-edge velocity $V_2(x_2,y_2,z_2)$
Competitions of migratory paths at different locations (x_1,y_1,z_1) (x_2,y_2,z_2)
Pore size for nucleus squeezing through
Decision-making for directional migration
Cell globally follows chemotactic cues to migrate by adapting its transient paths

825 **Fig. 4.** Directional cell migration is steered by a balanced relation between intracellular
826 proteins, HTECMs and chemotactic cues. (*A*) Demonstration of initial simulation
827 conditions that local leading edges drive cell migration at the two locations of $\mathbf{x}_1$ and $\mathbf{x}_2$.
828 Yellow and violet arrows denote the migration directions at $\mathbf{x}_1$ and $\mathbf{x}_2$, respectively. The
829 dots represent chemoattractant of actin. (*B*) Local extracellular resistance of ECMs and
830 local concentration of actin monomers caused by a gradient chemoattractant at the
831 positions of $\mathbf{x}_1$ and $\mathbf{x}_2$ in cases A-C. Migration distances (*C, E* and *G*) and leading-edge
832 actin cytoskeleton densities (*D*, *F* and *H*) in cases A-C (n=4). (I) Leading-edge migration
833 velocity for varying ECM resistance and actin concentration. (*J*) Directional cell
834 migration is steered by a balanced relation between intracellular proteins for assembling
835 leading-edge actin cytoskeleton, local resistances of HTECMs and chemotactic cues.

836

Table 1. RAP model systematically predicts all the key adaptive migratory behaviours discovered in experiments.

Key lamellipodial leading edge behaviours during cell migrations	Corresponding modeling results
1. Adaptive propulsive force generation based on ECM resistance (1)	Fig. 2*E* and 2*F*
2. The orientation of actin filaments in lamellipodial is about ±35° relative to the migration direction (1, 52).	Fig. 2*C*
3. Increased ECM resistance induces the increase of branched actin filament density (1, 5, 11).	Fig. 2*A*
4. Increased resistance induces the decrease in the rates of actin nucleation and capping of barbed ends (25).	Fig. 3*F*
5. Increased resistance induces the decrease in the rates of Arp2/3 branching (25).	Fig. 3*G*
6. Overexpression of Arp2/3 complex is positively related to cell migratory ability and velocity (15, 17, 62).	Fig. 2*A*, 2*B*, 2*E* and 2*F*
7. Increased ECM resistance leads to denser mitochondria at the Arp2/3 complex-assembled invasive cell leading edge and ATP can boost cancer leading edge invasion (11, 53).	Fig. 2*D*
8. Migratory leading edge can circumnavigate obstacles and select the path of least resistance (6).	Fig. 3*B*, 3*C*, 3*F* and 3*G*
9. Leading edge migration velocity depends on extracellular resistance history (1, 26).	Fig. 2*H*
10. VASP promotes actin filament elongation and thus improves cell migration velocity (60).	Supplementary Fig. 7